

## Turbulence and Radiation in Stratocumulus-Topped Marine Boundary Layers: A Case Study from VOCALS-REx

VIRENDRA P. GHATE\*

*Department of Environmental Sciences, Rutgers, The State University of New Jersey, New Brunswick, New Jersey*

BRUCE A. ALBRECHT

*Division of Meteorology and Physical Oceanography, University of Miami, Miami, Florida*

MARK A. MILLER

*Department of Environmental Sciences, Rutgers, The State University of New Jersey, New Brunswick, New Jersey*

ALAN BREWER AND CHRISTOPHER W. FAIRALL

*Physical Sciences Division, NOAA/Earth System Research Laboratory, Boulder, Colorado*

(Manuscript received 14 August 2012, in final form 30 July 2013)

### ABSTRACT

Observations made during a 24-h period as part of the Variability of the American Monsoon Systems (VAMOS) Ocean–Cloud–Atmosphere–Land Study Regional Experiment (VOCALS-REx) are analyzed to study the radiation and turbulence associated with the stratocumulus-topped marine boundary layer (BL). The first 14 h exhibited a well-mixed (coupled) BL with an average cloud-top radiative flux divergence of  $\sim 130 \text{ W m}^{-2}$ ; the BL was decoupled during the last 10 h with negligible radiative flux divergence. The averaged radiative cooling very close to the cloud top was  $-9.04 \text{ K h}^{-1}$  in coupled conditions and  $-3.85 \text{ K h}^{-1}$  in decoupled conditions. This is the first study that combined data from a vertically pointing Doppler cloud radar and a Doppler lidar to yield the vertical velocity structure of the entire BL. The averaged vertical velocity variance and updraft mass flux during coupled conditions were higher than those during decoupled conditions at all levels by a factor of 2 or more. The vertical velocity skewness was negative in the entire BL during coupled conditions, whereas it was weakly positive in the lower third of the BL and negative above during decoupled conditions. A formulation of velocity scale is proposed that includes the effect of cloud-top radiative cooling in addition to the surface buoyancy flux. When scaled by the velocity scale, the vertical velocity variance and coherent downdrafts had similar magnitude during the coupled and decoupled conditions. The coherent updrafts that exhibited a constant profile in the entire BL during both the coupled and decoupled conditions scaled well with the convective velocity scale to a value of  $\sim 0.5$ .

### 1. Introduction

Marine stratocumulus clouds have significantly higher albedo than the underlying ocean surface, and when present, they reflect greater amounts of incoming solar radiation back to space. Because of their low cloud-top

heights, the longwave radiation emitted by these clouds is comparable to that emitted by the ocean surface, whereupon they produce a minimal impact on the top-of-the-atmosphere (TOA) longwave radiation energy budget. The net radiative effect of these clouds is to cool the ocean surface. Vast layers of stratocumulus clouds are observed over the eastern subtropical oceans with the largest subtropical stratocumulus layer present over the southeast Pacific Ocean region west of the coasts of Chile and Peru (Klein and Hartmann 1993). These extensive stratocumulus layers impose overcast skies upon a large area of the ocean surface and thereby impart a significant influence on the Earth's radiation budget,

---

\* Current affiliation: Division of Environmental Sciences, Argonne National Laboratory, Argonne, Illinois.

---

Corresponding author address: Virendra P. Ghate, 9700 South Cass Ave., Argonne, IL 60439.  
E-mail: vghate@anl.gov

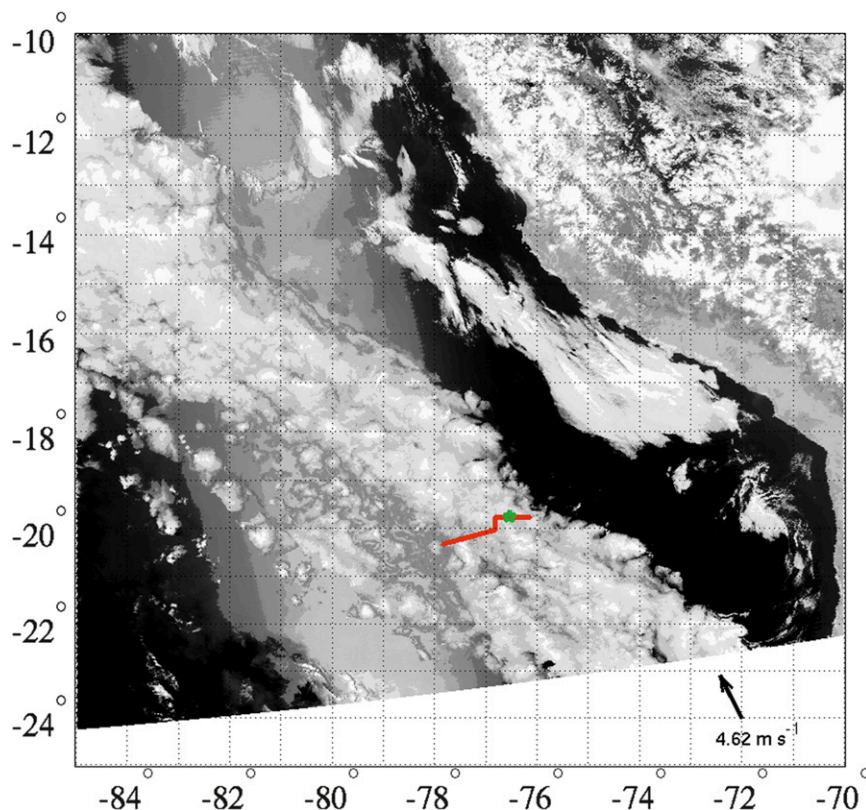


FIG. 1. Visible image as captured by the MODIS *Aqua* satellite on 27 Nov 2008 at 1855 UTC (1255 LT). The red line shows the eastward track of the R/V *Ronald H. Brown* for that day.

making it essential to represent these clouds and the associated processes accurately in global climate model (GCM) simulations aimed at predicting the future climate. However, these clouds occur at spatial scales that are poorly resolved by GCMs; thus, their cloudiness and associated effects need to be parameterized, and many parameterizations have been proposed for this purpose (e.g., Klein and Hartmann 1993; Bretherton et al. 2004). While cumulus parameterizations in GCMs perform admirably in some circumstances and in some regions, they misrepresent marine stratocumulus in many others and remain a major source of uncertainty in the climate forecasts (Bony and Dufresne 2005).

Marine stratocumulus clouds are intrinsically linked to turbulence in the marine boundary layer (BL), and many observational (e.g., Frisch et al. 1995; Ghate et al. 2010) and modeling studies (Mechem et al. 2012; Zhu et al. 2005; Stevens et al. 1999; Moeng et al. 1996) have focused on this link. Turbulent kinetic energy generation in the stratocumulus-topped marine BL is maintained through radiative cooling near cloud top, which mainly occurs in the longwave (LW) radiation spectral band (Lilly 1968). This LW radiative cooling can be offset during the daytime by radiative heating resulting from the absorption of

shortwave (SW) radiation by water vapor and cloud droplets, and with insufficient turbulent kinetic energy generation to mix the full depth of the marine BL, it becomes stratified into two isolated layers—this is known as decoupling. This decoupling of the cloud layer from its subcloud layer prevents moisture resupply to the cloud layer, potentially leading to its thinning or dissipation during the daytime. This decoupling phenomenon is not captured well in GCMs because of inadequate representation of the cloud–radiation–turbulence interactions (Medeiros et al. 2012).

Decoupled BLs were routinely observed during the Variability of the American Monsoon Systems (VAMOS) Ocean–Cloud–Atmosphere–Land Study Regional Experiment (VOCALS-REx; Wood et al. 2011; Jones et al. 2011; Bretherton et al. 2010), and we use these data to study the differences in the BL turbulence structure during coupled and decoupled episodes. Data collected on board the R/V *Ronald H. Brown* on 27 November 2008 are the foundation of the present study. Satellite imagery captured by the Moderate Resolution Infrared Spectroradiometer (MODIS) on board the *Aqua* satellite during the study period and the eastward track of the R/V *Ronald H. Brown* are shown in Fig. 1. Also shown in Fig. 1 is the

location of the R/V *Ronald H. Brown* when the satellite image was captured. Since the image was taken later during the day, the ship sampled closed cells for most of the day and then made a transition to an open cellular BL structure toward the end of the day. The ship's speed was  $\sim 6 \text{ m s}^{-1}$  during the first 2 h,  $0 \text{ m s}^{-1}$  from 0200 to 0400 UTC, and about  $2 \text{ m s}^{-1}$  during the rest of the study period. The mean speed of the R/V *Ronald H. Brown* during the day was  $2.44 \text{ m s}^{-1}$ . Instrumentation on board the R/V *Ronald H. Brown* is described in detail by Wood et al. (2011), and hence, we have only described the subset of the instrumentation on board the R/V *Ronald H. Brown* used in this study. In the next section, the instrumentation along with the radiative transfer model is described, which is followed by a section describing the general conditions during the study period. The data are then further classified as coupled and decoupled based on the thermodynamic structure, and statistics for this classification are presented in section 4. The article is concluded with a summary and discussion section.

## 2. Instrumentation and radiative transfer model

The instrumentation suite present on board the R/V *Ronald H. Brown* included a motion-stabilized, vertically pointing Doppler cloud radar, a motion-stabilized scanning Doppler lidar, a laser ceilometer, a microwave radiometer, and a turbulent–radiative flux suite. Balloon-borne radiosondes were also launched every 4 h. A 95-GHz cloud radar was operated exclusively in vertically pointing mode (Moran et al. 2012) and recorded the Doppler spectrum and its first three moments: reflectivity, mean Doppler velocity, and Doppler spectrum width. The radar was operating at a 3-Hz and 20-m temporal and spatial resolution, respectively. A high-resolution Doppler lidar (HRDL) operating at  $2\text{-}\mu\text{m}$  wavelength (Grund et al. 2001; Tucker et al. 2009) was pointing vertically for 10 min and scanning either in a range height indicator (RHI) or plan position indicator (PPI) mode for the other 10 min in alternate cycles. The HRDL recorded the aerosol backscatter signal strength and Doppler velocity at 2-Hz sampling frequency and 30-m range gate spacing. The HRDL data from the vertically pointing mode only are used in this study. A 905-nm wavelength laser ceilometer was used to measure the first three optical cloud-base heights at 15 s and 15-m resolution. Broadband radiometers recorded the downwelling shortwave radiation ( $0.3\text{--}3\ \mu\text{m}$ ) and downwelling longwave radiation ( $4\text{--}50\ \mu\text{m}$ ) each minute. Accompanying these instruments was a flux suite accumulating high temporal resolution temperature, wind, and humidity measurements used to calculate the surface sensible heat flux (SHF) and latent heat flux (LHF) according to the technique described by

Fairall et al. (2003). A microwave radiometer (MWR) recorded the sky brightness temperatures at 23.8 and 31.4 GHz, from which the atmospheric column integrated water vapor (IWV) and liquid water path (LWP) were estimated every 30 s (Zuidema et al. 2005).

Radiative heating rate profiles were computed every second using the rapid radiative transfer model (RRTM; Mlawer et al. 1997; Mlawer and Clough 1998) using radiosonde moisture and temperature measurements and measurement-constrained cloud microphysical properties similar to Mather et al. (2007). These simulations possessed a resolution of 20 m from the surface to 1.5 km, 500 m from 1.5 to 12 km, and 1 km from 12 to 60 km. Greenhouse gas concentrations were supplied to RRTM based upon the latest measurements, most notably a carbon dioxide concentration of 388.5 ppm. Because of inadequate information about the aerosol properties, radiative effects due to aerosols were neglected in the RRTM simulations; however, the remote ocean location and overcast nature of the study area likely justifies their exclusion in our study (Tomlinson et al. 2007). The temperature and humidity profiles from the closest radiosonde were used in the calculations. The cloud liquid water content (LWC) was determined using the radar reflectivity per the formulation put forward by Liao and Sassen (1994). Based on the review of in situ measurements by Miles et al. (2000), the cloud droplet effective radius was calculated from the determined LWC assuming a lognormal drop size distribution with total cloud drop number concentration of  $100 \text{ cm}^{-3}$  and drop size distribution width of 0.35. The radiative effects of precipitation were neglected in the model. The temperature and humidity profiles from the closest radiosonde were used in the calculations. Accounting for cirrus clouds in the RRTM simulations was problematic because the maximum observation range of the radar and HRDL were 4 and 6 km, respectively, but none of the soundings launched during the day showed an increased relative humidity at high levels that would have been indicative of cirrus, and they were neglected in the RRTM simulations. Also, the satellite imagery (Fig. 1) during the day did not show any cirrus clouds. Since we are invoking the independent pixel approximation by using a one-dimensional radiative transfer model, we neglect any three-dimensional radiative effects. Since the conditions observed during this case study are of a single-layer stratocumulus cloud or of clear sky periods, we anticipate the 3D effects to be minimal.

## 3. Case description

The radar-observed reflectivity and mean Doppler velocity for 27 November 2008 are shown in Fig. 2 along

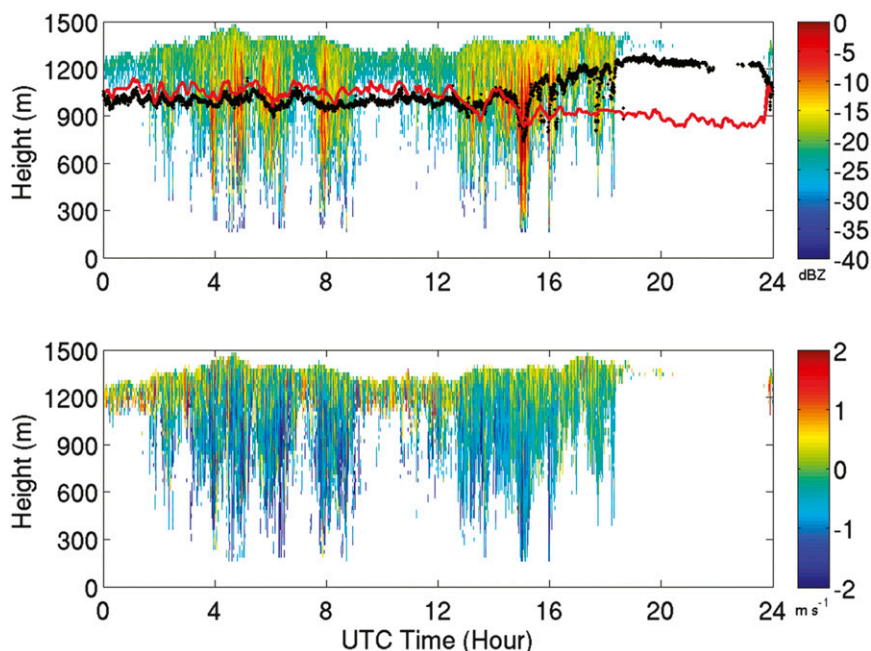


FIG. 2. (top) Reflectivity (dBZ) and (bottom) mean Doppler velocity ( $\text{m s}^{-1}$ ) as recorded by the vertically pointing 95-GHz Doppler cloud radar on 27 Nov 2008. The ceilimeter-recorded cloud-base height is shown in black while the lifting condensation level calculated using surface measurements is shown in red.

with the lifting condensation level (LCL) calculated using surface meteorological measurements per the formulation by Bolton (1980) and the ceilimeter-observed lowest cloud-base height. The local time is 6 h behind coordinated universal time (UTC). Variability is evident throughout the day in these observations, as indicated by systematic excursions in the cloud-top height over periods of several hours. A thin stratus layer was detected by the ceilimeter from 1800 to 0000 UTC, but was undetected by the cloud radar because of its lower sensitivity (higher cloud detection threshold signal-to-noise ratio). Intermittent evaporating precipitation into the subcloud layer can be seen as negative Doppler velocities below the ceilimeter cloud base that were detected from 0400 to 0900 UTC and from 1300 to 1600 UTC. The optical rain gauge did not detect any precipitation at the surface during the 24-h study period, suggesting that most of the precipitation evaporated before reaching the surface. Excellent correspondence between the ceilimeter-detected cloud-base height and the LCL was noted from 0000 to 1400 UTC, after which the two levels differed from each other. Such a thermodynamic structure is symptomatic of a BL that was well mixed and coupled to the surface (Jones et al. 2011) from 0000 to 1400 UTC and decoupled thereafter. A rapid increase in the LCL toward the last 10 min of the 24th hour is noteworthy, but the BL was decoupled

for the majority of that hour, and these final 10 min are inconsequential to the statistics presented in this study.

The HRDL-recorded aerosol backscatter and Doppler velocity and the ceilimeter-observed first cloud-base height are shown in Fig. 3. Attenuation by cloud droplets prevents the HRDL from penetrating significantly above the optical cloud base, thereby limiting its sampling to the subcloud layer only. Since only the data from the vertically pointing mode are shown, data gaps correspond to the periods when the HRDL was performing RHI or PPI scans. As the cloud layer thinned after 1800 UTC, and especially during the clear sky conditions observed during 2200 UTC, the HRDL was able to observe the entire BL. Backscatter decreased after 1800 UTC, suggesting lower aerosol concentration during this period, perhaps due to scavenging by precipitation, though a definitive cause for this decrease cannot be determined from these observations.

Profiles of potential temperature and mixing ratio from six radiosondes launched 4 h apart (Fig. 4) depict a nearly constant inversion-base height during the day that corresponded well to the average cloud-top heights observed by the cloud radar in the vicinity of radiosonde launch times. Except for the radiosonde launched on 0800 UTC, all the soundings showed relatively constant potential temperature and mixing ratio profiles, especially in the subcloud layer, though the 2000 UTC sounding

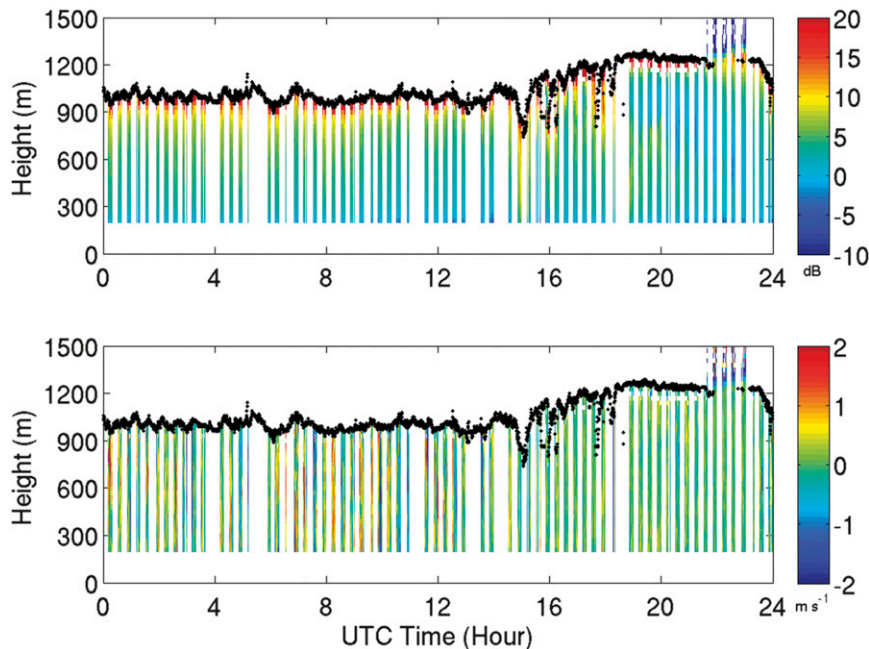


FIG. 3. (top) The signal-to-noise ratio and (bottom) Doppler velocity ( $\text{m s}^{-1}$ ) as recorded by the HRDL when it was pointing vertically upward on 27 Nov 2008. The ceilometer-recorded cloud-base height is shown in black.

indicated decoupling with a weak inversion around 850 m. This inversion coincided with the LCL during that hour (850 m), confirming that the cloud layer was thermodynamically decoupled from the subcloud layer. A weak inversion can also be seen in the sounding launched at 1600 UTC at around 900 m. The BL winds were from the southwest as reported by all of the soundings, with little variations in the wind speed with height (not shown). There was no significant change noticed in either the wind speed or the wind direction near the LCL in all the soundings, including the 2000 UTC sounding, which showed distinct decoupled layers.

The case-mean profile of the longwave radiative flux, shortwave radiative flux, and net radiative flux as simulated by RRTM is shown in Fig. 4, along with the associated heating rate profiles. A positive value of flux denotes a net downward flux, while a negative value denotes a net upward flux. The longwave flux was almost constant with height in the subcloud layer and in the free troposphere but showed a slight increase with height near cloud base and a sharp decrease with height near cloud top. This decrease of the longwave flux above cloud top is indicative of cloud droplet and moisture gradient present near the boundary layer inversion, causing a decrease in the downwelling LW flux. Absorption of shortwave radiation by water vapor caused the shortwave flux to increase slightly from the surface toward cloud base and from cloud base to the cloud top with a constant

profile in the free troposphere. Predictably, the longwave radiative flux was negative in the entire troposphere, the shortwave radiative flux was positive, and the net radiative flux was also positive. Net radiative fluxes were about  $150 \text{ W m}^{-2}$  in the subcloud layer and about  $100 \text{ W m}^{-2}$  in the free troposphere, and the net radiative flux showed a slight increase in the cloud layer and a sharp decrease near the BL inversion.

Radiative flux profiles produced longwave heating rates that were weakly positive near cloud base and strongly negative ( $\sim 3.5 \text{ K h}^{-1}$ ) near cloud top. The zig-zag structure of the LW heating rate in the middle of the cloud layer is an artifact of averaging samples with different cloud thickness rather than changes in radiation. Shortwave heating rate increased from the cloud base to the cloud top with a sharp decrease above that. Consequently, net radiative heating loosely echoed the profile of longwave radiative heating with a diminished magnitude. All of the radiative heating rates were almost zero in the subcloud layer and above the BL inversion. These radiative fluxes and heating rate profiles are in general agreement with previous modeling (Moeng et al. 1996; Stevens et al. 1999) and observational studies (Duda et al. 1991) in marine stratocumulus clouds.

Downwelling LW radiation at the surface during the study period (Fig. 5) was constant throughout the day with a decrease observed between 2100 and 2300 UTC as the cloud layer thinned and eventually disappeared.

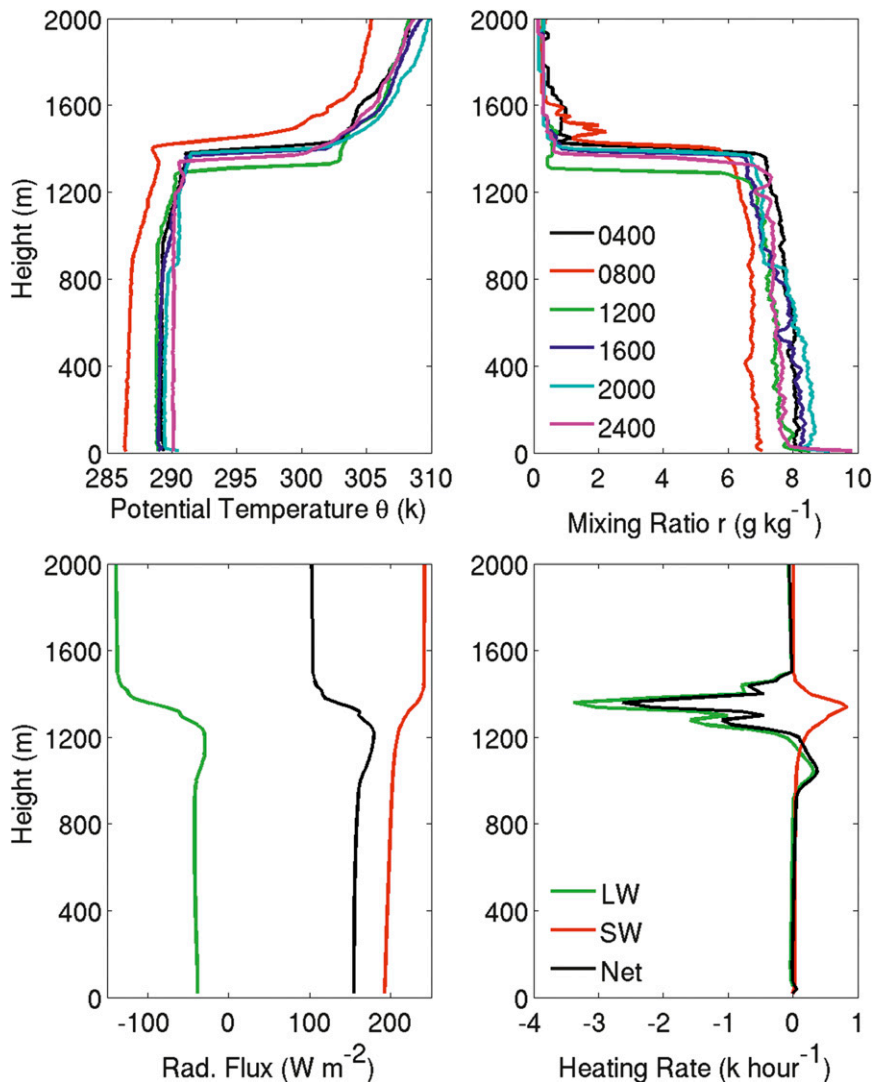


FIG. 4. (top) Profiles of (left) potential temperature and (right) mixing ratio as measured by the radiosondes launched during that day and (bottom) profiles of averaged (left) LW, SW, and net radiative flux along with (right) the associated heating rates.

Downwelling SW radiation loosely followed the insolation exhibiting variability typically associated with passing clouds, although changes in the cloud microphysical properties might also have contributed to this variability. The surface LHF (Fig. 5) exceeded  $60 \text{ W m}^{-2}$ , except when it decreased sporadically between 0500 and 0900 UTC. A plausible explanation for these decreases is an increase in the surface specific humidity due to drizzle evaporation during those times (see Fig. 2). The SHF was always negligibly low:  $<6 \text{ W m}^{-2}$ , with a peak around 1300 UTC. Predominance of the LHF over SHF in this region is in agreement with the previous long-term observations (Ghate et al. 2009; de Szoeke et al. 2012).

Column IWV as recorded by a microwave radiometer remained fairly constant around  $1.3 \text{ cm}$  throughout the

entire day while the LWP varied, with peaks corresponding to periods of changes in the cloud depth. A peak value of LWP of  $400 \text{ g m}^{-2}$  corresponded with the heaviest drizzle event, with most of the other relative peaks also associated with the precipitation events. Coincidence between LWP and drizzle intensity is circumstantially supportive of the relation between precipitation and the LWP (Caldwell and Bretherton 2009). Although no cloud layer was present from 2200 to 2300 UTC, the radiometer recorded an LWP of  $80 \text{ g m}^{-2}$  corresponding to a bias in the retrieval of LWP from the MWR.

The surface buoyancy flux  $B$  was calculated using the SHF, LHF, air density  $\rho$ , and specific heat of the air  $c_p$  using the following equation and is shown in Fig. 6:

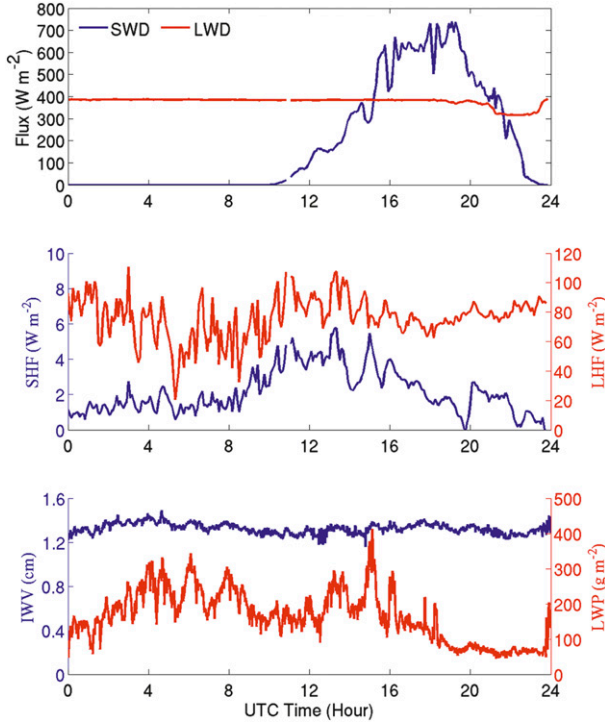


FIG. 5. (top) Downwelling SW and LW radiation, (middle) surface sensible and latent heat flux, and (bottom) IWV and LWP for 27 Nov 2008.

$$B = \rho \times c_p \times (\overline{w'\theta'_v}).$$

It closely follows the SHF with a minimum of  $\sim 2 \text{ W m}^{-2}$ , a maximum of  $\sim 13 \text{ W m}^{-2}$ , and an average value of  $7.65 \text{ W m}^{-2}$ . Hence, the buoyancy production at the surface varied little during the entire day. In addition to  $B$  generating convection at the surface through heating of air parcels, radiative cooling predominantly in the upper half of the BL also generates convection through cooling of the air parcels. The shortwave, longwave, and net radiative divergence  $\Delta F_{\text{rad}}$  from the surface to boundary layer inversion base are shown in Fig. 6. During nighttime, the longwave radiative divergence is relatively constant at around  $-110 \text{ W m}^{-2}$ , while during the daytime, because of absorption of solar radiation by water vapor and cloud droplets, the net divergence increased to a value above zero (heating) around 1500 UTC (0900 LT). The net radiative divergence was above zero until 2100 UTC (1500 LT), with a drop around 2000 UTC due to the disappearance of the cloud layer. Although the cloud layer was only intermittently present after 2000 UTC, the LW divergence was about  $-50 \text{ W m}^{-2}$  mainly because of the jump in mixing ratio across the BL inversion.

The surface convective velocity scale  $w_{\text{sfc}}^*$  was also calculated using the following equation per Stull (1988),

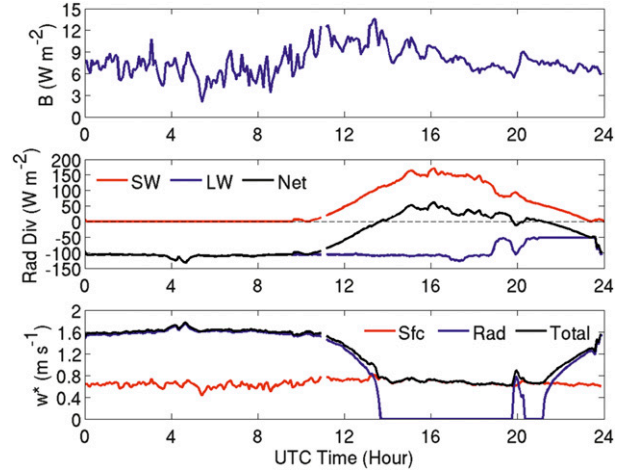


FIG. 6. (top) Surface buoyancy flux; (middle) SW, LW, and net radiative divergence; and (bottom) convective velocity scale for the entire day.

which uses the BL inversion-base height  $Z_i$  as the scaling height along with the acceleration due to gravity  $g$  and the surface virtual potential temperature  $\bar{\theta}_v$ :

$$w_{\text{sfc}}^* = \left[ \frac{g \times Z_i}{\bar{\theta}_v} \times (\overline{w'\theta'_v})_{\text{sfc}} \right]^{1/3}.$$

The  $w_{\text{sfc}}^*$  varied little during the period (Fig. 6) with a mean value of  $\sim 0.65 \text{ m s}^{-1}$ . The cloud-top height, which was used as a proxy for the inversion-base height, varied little during the study period, as did the buoyancy flux (discussed earlier), and further, because of the one-third power dependence, there was little change in  $w_{\text{sfc}}^*$ .

Lock and MacVean (1999) proposed a complementary radiative velocity scale  $w_{\text{rad}}^*$ , which used the change in the radiative flux over the entire boundary layer and the boundary layer depth as a scaling height. Their formulation was based on the original results by Bohnert (1993), who proposed the  $w_{\text{rad}}^*$  formulation for clear-air boundary turbulence. We have used the Lock and MacVean (1999) formulation, which uses  $Z_i$ ,  $\rho$ ,  $c_p$ , and mean potential temperature of the BL  $\bar{\theta}$  to calculate  $w_{\text{rad}}^*$ . The air density was assumed to be constant at  $1.2 \text{ kg m}^{-3}$ :

$$w_{\text{rad}}^* = \left[ \frac{g \times Z_i}{\rho \times c_p \times \bar{\theta}} \times (-\Delta F_{\text{rad}}) \right]^{1/3}.$$

Based on aircraft measurements, Tjernström and Rogers (1996) proposed a similar formulation using the buoyancy flux at the cloud top and cloud thickness as a scaling height. The value of  $w_{\text{rad}}^*$  was  $\sim 1.55 \text{ m s}^{-1}$  during the

nighttime and decreased to zero around 1500 UTC. Except for a few wiggles, it remained zero until 2200 UTC (1600 LT). Although no cloud layer was present during 2300 UTC, because of a low amount of heating in the SW spectrum but significant cooling in the LW spectrum,  $w_{\text{rad}}^*$  was around  $1.2 \text{ m s}^{-1}$ .

The surface convective velocity scale and the radiative velocity scale were combined to yield the total velocity scale (velocity scale from here on), which is the cubic sum of the two:

$$w^{*3} = w_{\text{sfc}}^{*3} + w_{\text{rad}}^{*3}.$$

This velocity scale  $w^*$  was over  $1.6 \text{ m s}^{-1}$  during the nighttime and decreased to a value of  $\sim 0.6 \text{ m s}^{-1}$  during the daytime. Since the radiative cooling and surface heating of air is taken into account in the formulation of the velocity scale, it presents an opportunity to have a scaling variable for dynamical parameters under a variety of conditions. However, we acknowledge that drizzle evaporative cooling can also be a factor in controlling the BL dynamics (Ackerman et al. 2009), and the current formulation of  $w^*$  does not take it into account.

The surface buoyancy flux and the cloud-top radiative cooling drive the turbulence in the BL. Although the driving forces and the associated mechanisms in a stratocumulus-topped BL are well understood, the extent to which the parcels affected by these forces travel (length scale) is not. The turbulence in a stratocumulus-topped marine BL is mainly cloud-top driven and hence, during thermodynamically coupled conditions, the entire BL depth might be a suitable length scale for  $w_{\text{rad}}^*$  and during thermodynamically decoupled conditions, the distance between the cloud top and the LCL be a suitable scale length for  $w_{\text{rad}}^*$ . We have chosen the BL inversion-base height as the length scale in the calculation of both  $w_{\text{sfc}}^*$  and the  $w_{\text{rad}}^*$ , as updrafts and downdrafts spanning through the entire BL from the surface to cloud top were observed during both coupled and decoupled conditions (discussed later). Further, our aim was to propose a definition of  $w^*$  generic enough to be applicable to GCMs, which have difficulty in differentiating between coupled and decoupled BLs. Although the choice of the length scale affects the magnitude of  $w^*$ , the scaling results presented later (Fig. 15) did not experience a significant change with any of the choices of the length scale discussed above.

#### 4. Data processing and case-mean statistics

Data from the Doppler cloud radar and HRDL were averaged to produce a 1-Hz, 30-m uniform grid for further processing. The backscatter signal from the HRDL

operating at  $2\text{-}\mu\text{m}$  wavelength is sensitive to aerosols that have negligible fall velocity and therefore act as tracers of the vertical wind, so the HRDL Doppler velocity tracked the air vertical motion. During drizzle events, it is possible for the HRDL to record the drizzle fall velocity rather than the air motion. But the mean HRDL-recorded vertical velocity for every 10 min was very close to zero at all levels. Further, both updrafts and downdrafts were recorded in the subcloud layer by the HRDL during drizzle events, suggesting minimal impact of drizzle fall velocity on the HRDL Doppler velocity. However, some effect of precipitation drops on the HRDL recorded vertical velocity cannot be completely ruled out.

Cloud radar operating at 95 GHz is sensitive to cloud and precipitation size droplets. Since the cloud droplets have negligible fall velocity, the Doppler velocity during cloud-only conditions ( $< -20 \text{ dBZ}$ ) represented air motions (Frisch et al. 1995; Ghate et al. 2010). Precipitation fall velocity must be subtracted from the observed Doppler velocity to determine the air vertical motion and, among the several published techniques that may be applied (Kollias et al. 2011), we chose a technique similar to Feingold et al. (1999) and Frisch et al. (1995). A cubic fit between reflectivity and mean Doppler velocity was computed for 5-min averaging windows, and this fit was assumed to represent the contribution from fall velocity. The fall velocity yielded by the empirical fit was then subtracted from the 1-Hz observed Doppler velocity to yield the vertical air motion. We acknowledge that this approach inherently neglects any correlation between the vertical air motion and the reflectivity as reported by Vali et al. (1998), Lothon et al. (2005), Comstock et al. (2004), and others. However, more recently for cumulus and stratocumulus clouds, Ghate et al. (2011) have demonstrated lack of correlation between the air motion and reflectivity. Further, the vertical velocity from cloud radar was only retrieved above the ceilometer-detected cloud-base height, limiting the presence of drizzle drops. The scatterplots between the radar recorded mean Doppler velocity and reflectivity (not shown) demonstrated negligible correlation between the two near cloud top and a weak correlation near cloud base while the scatterplots between the radar reflectivity and retrieved vertical air motion (not shown) did not demonstrate any correlation between the two at all levels. Also, the range (spread) of retrieved vertical velocity was similar, around  $0 \text{ m s}^{-1}$  for particular value of reflectivity, further suggesting that turbulent motions were retrieved from the radar data as suggested by Kollias and Albrecht (2000). While it is beyond the scope of this study to test the accuracy of the retrieval technique or to compare it with other techniques in the literature, the profiles of the

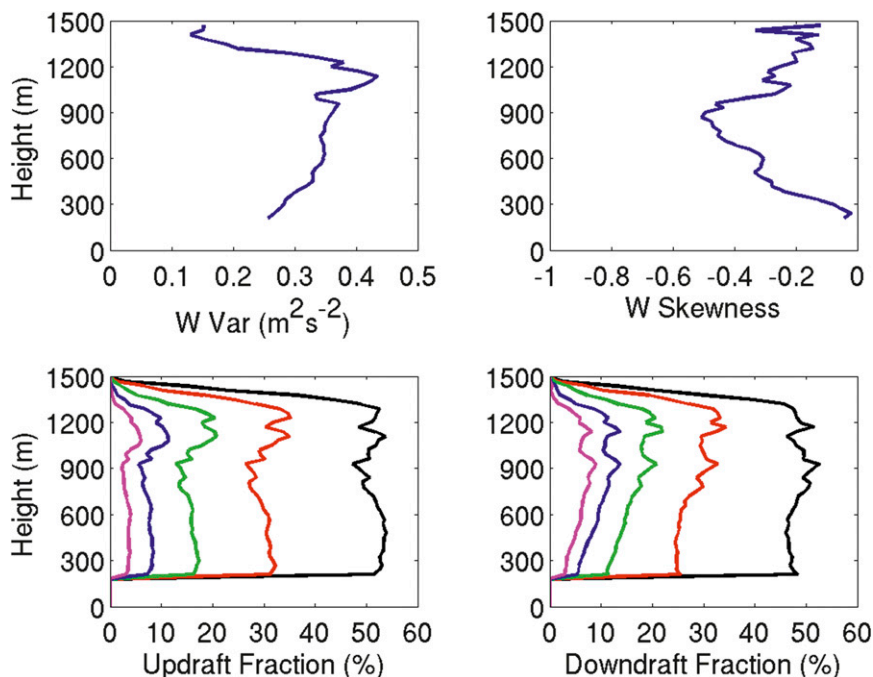


FIG. 7. Averaged profiles of (top left) vertical velocity variance and (top right) vertical velocity skewness. The (bottom left) updraft and (bottom right) downdraft fractions are shown with thresholds of 0 (black), 0.25 (red), 0.50 (green), 0.75 (blue), and 1 (magenta)  $\text{m s}^{-1}$ . The thresholds are similar in magnitude but negative for the downdraft fraction.

vertical velocity and related parameters showed convincing consistency below and above the cloud base, although they were retrieved through different techniques. The average cloud-base height was 1052 m and LCL was 990 m during the study period.

Vertical velocity profiles from near the surface to the top of the cloud layer for every second were constructed by combining the HDRL and cloud radar measurements using the ceilometer cloud-base height as the terminus of the HDRL profile and the beginning of the cloud radar profile. Further, because of the possibility of low-frequency (more than 30 min) drift in vertical motion correction and pointing angle stabilization, the hourly mean vertical velocity was subtracted from the retrieved velocities at each level. These hourly mean values were less than  $0.1 \text{ m s}^{-1}$  at all levels during the day.

The level of BL turbulence is reflected in the average vertical velocity variance and its skewness, which are shown in Fig. 7. Vertical velocity variance increased from  $0.25$  to  $0.45 \text{ m}^2 \text{ s}^{-2}$  from 200 m until its peak at 1100 m and decreased toward cloud top. Negative vertical velocity skewness denoted that downdrafts were stronger than the updrafts in the entire BL, with the difference between the two being greatest at 900 m. Structurally, this configuration indicates that the most turbulent region in the cloud consists of coexisting

updrafts and downdrafts, with a slight predisposition to contain some strong downdrafts while the region nearer to cloud base exhibits a considerably stronger predisposition to contain strong downdrafts, though it is less turbulent overall.

Conditionally sampled updraft and downdraft fractions (Fig. 7) reveal that in the lower half of the BL there are more updrafts than downdrafts, while in the upper half of the BL there are about an equal number of updrafts and downdrafts. The percentage of updrafts exceeding  $0.25 \text{ m s}^{-1}$  decreased from  $\sim 32\%$  at 200 m to  $\sim 27\%$  at 900 m but increased to above 30% above 900 m. Comparatively, the percentage of downdrafts stronger than  $-0.25 \text{ m s}^{-1}$  methodically decreased from  $\sim 30\%$  at cloud top to  $\sim 25\%$  at 200 m. In the BL as a whole, more downdrafts exceeded  $-1 \text{ m s}^{-1}$  than updrafts exceeded  $1 \text{ m s}^{-1}$ , and the percentage of these updrafts remained constant from 200 to 600 m at  $\sim 4\%$  and decreased to a minimum of 2% at 900 m. The percentage of updrafts stronger than  $1 \text{ m s}^{-1}$  and the vertical velocity variance coincidentally peaked at 1100 m ( $\sim 6\%$ ), suggesting modulation of this variance by updrafts. Downdrafts stronger than  $-1 \text{ m s}^{-1}$  increased in frequency from cloud top to a maximum of 9% at 900 m and then decreased almost linearly to 200 m. Coincident occurrence of a minima in the vertical velocity

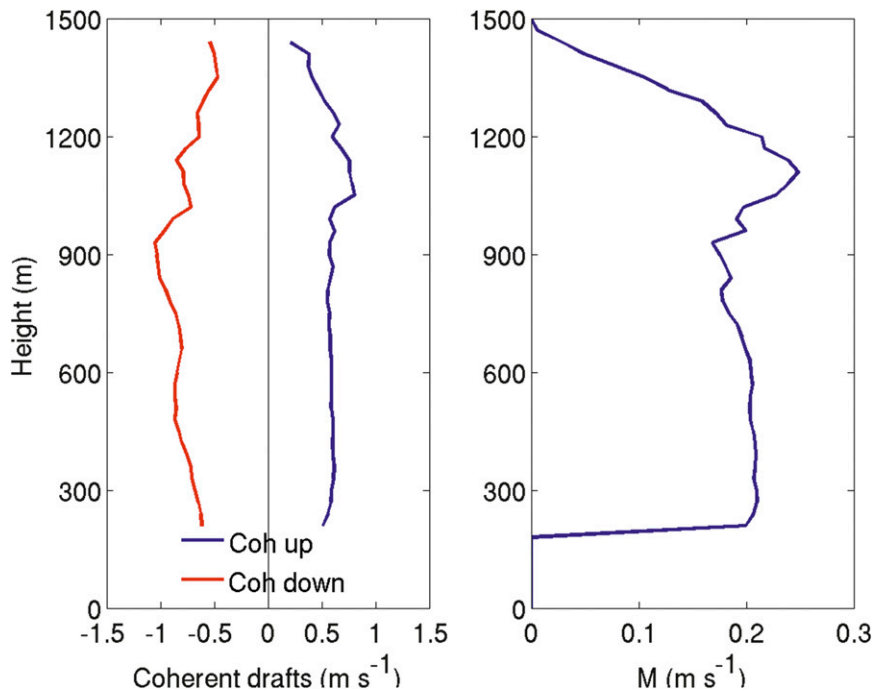


FIG. 8. (left) Averaged profiles of coherent updrafts and downdraft velocity and (right) averaged profile of updraft mass flux.

skewness and maxima in the downdrafts exceeding  $-1 \text{ m s}^{-1}$  at 900 m suggests that modulation of negative vertical velocity skewness is done primarily by the strongest downdrafts.

Updrafts and downdrafts that spanned the entire depth of the BL were defined as coherent and composite profiles of these features and are shown in Fig. 8. As only the sign of the vertical velocity and vertical extent was taken into account, the definition excludes slanted updrafts and downdraft structures. While the coherent updrafts experienced no acceleration and were almost constant at  $\sim 0.5 \text{ m s}^{-1}$  from 200 to 1000 m, with a small peak at 1000 m and decrease above, the coherent downdrafts experienced a more complicated acceleration and deceleration structure. Downdrafts accelerated as they sank from the cloud top to 900 m, where they peaked at  $-1.25 \text{ m s}^{-1}$  and steadily decelerated to about  $0.75 \text{ m s}^{-1}$  at 200 m. As only  $\sim 4\%$  of the updrafts and downdrafts were coherent, it occurs that the prevailing turbulent motions in the BL were discordant (disorganized).

Convective parameterizations employ the updraft-downdraft mass flux as a primary diagnostic variable, and the specific mass flux ( $M$ ) may be computed from these data using the classic plume decomposition technique proposed by Arakawa and Schubert (1974), which is given by

$$M = \sum_i \sigma_i \times (w_i - \bar{w}),$$

where  $w$  is the vertical velocity,  $\sigma$  is the updraft fraction, and  $\bar{w}$  is the hourly mean vertical velocity. Mass flux was calculated for each  $0.1 \text{ m s}^{-1}$  velocity bin from  $-3$  to  $3 \text{ m s}^{-1}$ , and these individual contributions to the total mass flux from each velocity bin are summed to produce the total mass flux at each height during each hour (the updraft component is summed from  $0$  to  $3 \text{ m s}^{-1}$ ). These hourly values were averaged to produce a composite profile of the updraft mass flux (Fig. 8), which loosely follows the profile of coherent updrafts. It remained constant from 200 to 1000 m at  $\sim 0.2 \text{ m s}^{-1}$  and exhibited a sharp increase leading to a maximum of approximately  $0.25 \text{ m s}^{-1}$  at 1100 m followed by a steady decline above.

To illustrate which velocity bins contribute the most to the total mass flux, the velocity binned mass flux at four levels is shown in Fig. 9 along with the updraft mass flux at each level. The updraft mass flux peak value exceeds that of the downdraft mass flux at each level, and eddies with velocity of  $\sim 0.5 \text{ m s}^{-1}$  are the predominant facilitators of the mass transport in the updraft regime at all levels. Downdraft eddies with velocity of  $-0.5 \text{ m s}^{-1}$  are responsible for most of the mass transport at 1200 m, while at 300 m the same is true for eddies with vertical velocity of  $-0.3 \text{ m s}^{-1}$ . Predictably, the tail of the distribution of

the downdraft mass flux is longer than that of the updraft mass flux at all levels given the negative vertical velocity skewness in the entire BL. Particularly, strong updraft eddies ( $>2 \text{ m s}^{-1}$ ) do not transport significant mass, while in contrast significant mass was transported by particularly strong downdraft eddies ( $<-2 \text{ m s}^{-1}$ ), especially at 900 m. The updraft and downdraft mass flux contributions are not entirely symmetrical about zero vertical velocity, and the most substantial asymmetry is the confinement of the updraft mass flux contributions to a more narrow range of velocities, which is indicated by the steep roll-off toward larger velocities when compared to the downdraft contributions. Apart from this velocity range asymmetry, the updraft mass flux is relatively constant at all four levels ( $\sim 0.2 \text{ m s}^{-1}$ ), except for a slight decrease at 900 m.

### 5. Coupled versus decoupled comparison

Hourly statistics were further classified as coupled and decoupled based on the separation between LCL height and cloud-base height. Hours with less than 100 m difference between hourly averaged value of LCL height and cloud-base height were labeled as coupled, while the hours with the difference between the LCL height and cloud-base height greater than 100 m were labeled as decoupled. This conditional sampling produced a clear bifurcation in the data in that the first 14 h were classified as coupled while the rest were classified as decoupled. The mean cloud-base height during coupled hours was 995 m, while the same during decoupled hours was 1148 m, and the LCL height during coupled hours was 1052 m, while the same during decoupled hours was 904 m. Average cloud-top heights for these two stability classifications were nearly constant (1330 and 1370 m), but there was a significant difference in the cloud thicknesses, which were 337 m during the coupled period and 265 m during the decoupled period. Mean values of parameters related to cloud macrophysical and BL thermodynamic properties during the entire case, coupled period, and decoupled period have been tabulated in Table 1. It should be noted that the periods when no clouds were present were excluded in the calculation of the cloud statistics. Jones et al. (2011) have used the difference between the potential temperature and mixing ratio values in the bottom 25% of the BL to the top 25% of the BL to diagnose decoupling using threshold values of 0.5 K and  $0.5 \text{ g kg}^{-1}$ . The mean (for all six soundings) potential temperature difference was 0.71 K while the mean mixing ratio difference was  $0.78 \text{ g kg}^{-1}$ . During the coupled conditions (first three soundings), the mean potential temperature difference between the bottom and top 25% of the BL was 0.72 K, while the

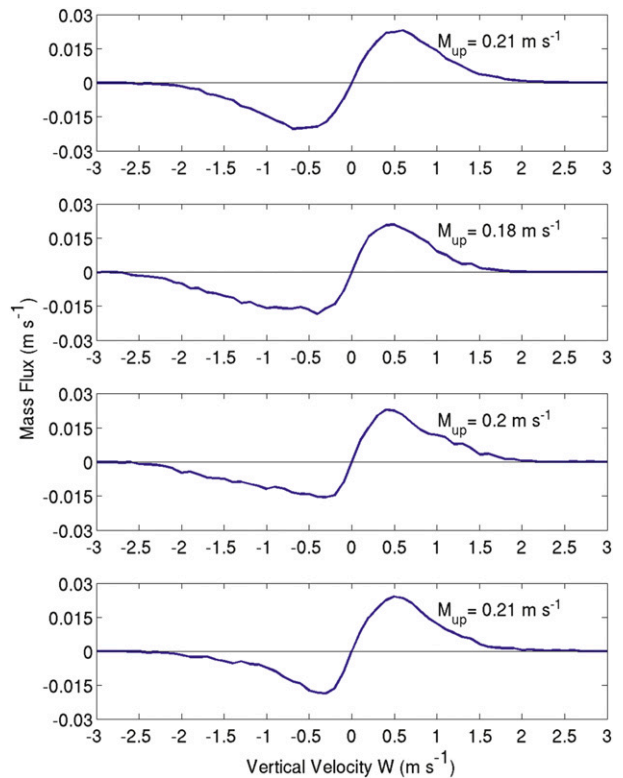


FIG. 9. Averaged profiles of velocity binned mass flux at (top to bottom) 1200, 900, 600, and 300 m. The updraft mass flux at each level is also reported in the respective panels.

same for mixing ratio was  $0.46 \text{ g kg}^{-1}$ . During decoupled conditions (last three soundings), the potential temperature and mixing ratio differences between the bottom 25% and the top 25% of the BL were 0.70 K and  $1.10 \text{ g kg}^{-1}$ , respectively. It is beyond the scope of this study to evaluate different criterion defining decoupling, but with the values of differences in the potential temperature and mixing ratio between the top and bottom 25% of the BL, it occurs that the BL was decoupled during the last 10 h of the study period. Also, mesoscale cellular convection might play a role in modulating the BL mixing as reported by Comstock et al. (2005) and Wood (2012), among others, but it is beyond the scope of this study to assess the impact of mesoscale cellular convection on BL mixing.

The radiation fluxes and the associated heating rates for the coupled and decoupled conditions are shown in Fig. 10. Consistent with past studies (Turton and Nicholls 1987; Bretherton and Wyant 1997), thermodynamic coupling was observed predominantly during the nighttime and in the early daylight hours when the shortwave radiation flux and associated heating rate were negligible. The net longwave flux during coupled conditions was around  $-30 \text{ W m}^{-2}$  in the subcloud layer, near zero in the cloud

TABLE 1. Mean values of variables during the entire case, coupled boundary layer conditions, and decoupled boundary layer conditions. Averaged values for the entire boundary layer of the parameters pertaining to the vertical velocity are reported.

Variable	Case mean	Coupled boundary layer	Decoupled boundary layer
Air temperature (°C)	17.86	17.74	18.04
Surface mixing ratio (g kg <sup>-1</sup> )	8.08	7.77	8.56
Sea surface temperature (°C)	18.54	18.45	18.66
Surface wind speed (m s <sup>-1</sup> )	4.41	4.02	4.98
Surface wind direction (°)	140	134	149
Integrated water vapor (cm)	1.32	1.32	1.31
Liquid water path (g m <sup>-2</sup> )	164	197	119
Sensible heat flux (W m <sup>-2</sup> )	2.14	2.25	2
Latent heat flux (W m <sup>-2</sup> )	75.82	74.54	77.61
Downwelling longwave radiation (W m <sup>-2</sup> )	377.20	385.27	365.95
Downwelling shortwave radiation (W m <sup>-2</sup> )	196.39	29.46	429.25
Lifting condensation level (m)	990	1052	904
Cloud-base height (m)	1052	995	1149
Cloud-top height (m)	1344	1322	1374
Cloud thickness (m)	316	337	265
Net heating rate at inversion base (K h <sup>-1</sup> )	-6.88	-9.04	-3.85
$w_{\text{slc}}^*$ (m s <sup>-1</sup> )	0.65	0.65	0.65
$w_{\text{rad}}^*$ (m s <sup>-1</sup> )	0.97	1.45	0.30
$w^*$ (m s <sup>-1</sup> )	1.21	1.52	0.79
Vertical velocity variance (m <sup>2</sup> s <sup>-2</sup> )	0.31	0.43	0.13
Vertical velocity skewness	-0.28	-0.36	-0.15
Coherent updrafts (m s <sup>-1</sup> )	0.59	0.71	0.41
Coherent downdrafts (m s <sup>-1</sup> )	-0.79	-0.97	-0.50
Percentage updrafts stronger than 1 m s <sup>-1</sup> (%)	2.69	4.22	0.32
Percentage downdrafts stronger than -1 m s <sup>-1</sup> (%)	4.32	6.37	1.14
Updraft mass flux (m s <sup>-1</sup> )	0.16	0.20	0.10

layer, and about  $-130 \text{ W m}^{-2}$  above the inversion base, whereupon the longwave heating rates were about  $0.5 \text{ K h}^{-1}$  near cloud base and about  $-3.5 \text{ K h}^{-1}$  near cloud top. As anticipated, net values of the radiation fluxes and heating rates echo those of longwave radiation.

Insolation substantially alters the radiation fluxes and the heating rates promoting thermodynamic decoupling. The longwave fluxes were  $-50 \text{ W m}^{-2}$  in the subcloud and cloud layer and about  $-150 \text{ W m}^{-2}$  above the BL inversion during decoupled conditions. Shortwave fluxes increased almost linearly from a surface value of  $425 \text{ W m}^{-2}$  to about  $450 \text{ W m}^{-2}$  near cloud base in response to water vapor absorption and exhibited a sudden increase to  $525 \text{ W m}^{-2}$  in the cloud layer and above the BL inversion. Net radiative fluxes during the thermodynamically decoupled conditions were positive with an average value of  $\sim 360 \text{ W m}^{-2}$  in the subcloud layer and above the BL inversion. The net radiation flux peaked near cloud top at  $\sim 400 \text{ W m}^{-2}$ , with the increase being rather gradual followed by a sudden decrease above the cloud top. Longwave radiative heating near cloud base was negligible during decoupled conditions, unlike the coupled conditions, while radiative cooling near cloud top remained nearly the same as that during coupled conditions ( $\sim -3.5 \text{ K h}^{-1}$ ). Shortwave radiative heating

rates increased from near zero just below cloud base to about  $1.8 \text{ K h}^{-1}$  near cloud top followed by a sharp decrease above to near zero. The net radiative heating increased from cloud base to a peak of  $1 \text{ K h}^{-1}$  in the middle of the cloud and then decreased sharply to a value of  $-2 \text{ K h}^{-1}$  near cloud top. Relative to the coupled conditions, the decoupled conditions had a higher amount of cloud-base heating and a lower amount of cloud-top cooling.

Vertical velocity variance and skewness during coupled hours and decoupled hours were averaged and the composites are presented in Fig. 11. Vertical velocity variances at all levels were higher when the BL was coupled and increased from 200 to 500 m and then remained constant to 1000 m. Above 1000 m, the coupled vertical velocity variances varied rather widely, though a signature feature is the peak at around 1150 m. In contrast, the vertical velocity variance is appreciably lower and nearly constant at  $\sim 0.15 \text{ m}^2 \text{ s}^{-2}$  in the entire boundary layer during the decoupled conditions. During coupled conditions, the vertical velocity skewness was negative in the entire BL and decreased from 200 m to its lowest value at 900 m, while above 900 m it increased to  $-0.1$  at 1150 m and remained fairly constant above that. The vertical velocity skewness associated with thermodynamic decoupling decreased from 200 to 800 m

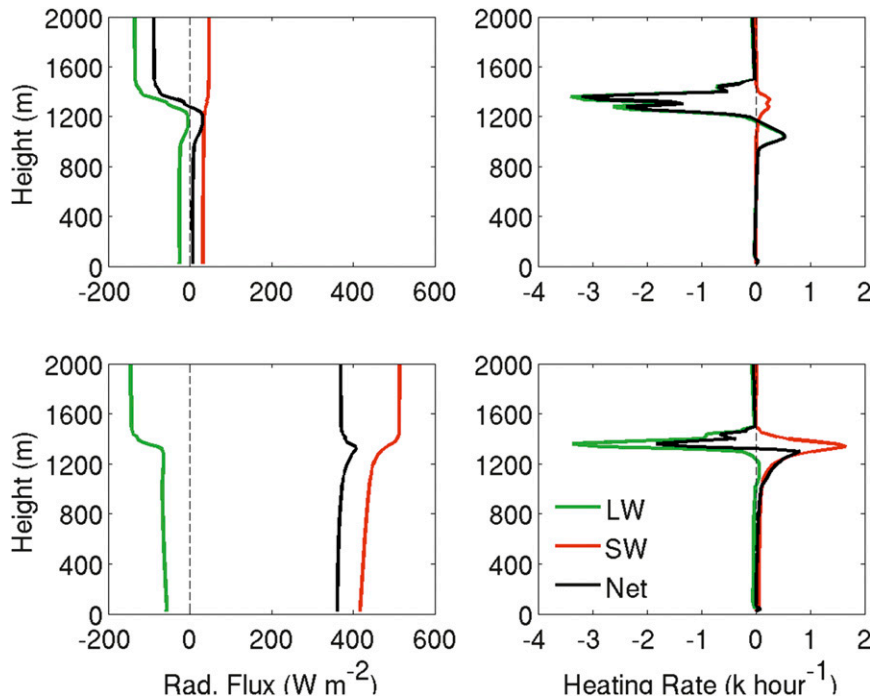


FIG. 10. (left) Radiative flux and (right) heating rate profiles during (top) coupled and (bottom) decoupled conditions.

and then remained fairly constant above that. Positive vertical velocity skewness from 200 to 500 m during decoupled periods is indicative of prevailing updrafts and suggests that the turbulent kinetic energy (TKE) is being generated by surface buoyancy, shear, and other processes near the ocean surface. The variance and skewness profiles for the coupled–decoupled distinction are similar to those reported by Hogan et al. (2009).

The conditionally sampled averaged updraft and downdraft fractions for coupled and decoupled conditions (Fig. 12) reveal differing patterns of organization at different levels in the BL, most notably in the subcloud layer because it is most affected by radiatively induced decoupling, evaporating drizzle, and shear-generated TKE at the ocean surface. Significant height-dependent variations in the subcloud layer are obvious in the thermodynamically coupled BL, but less obvious in the decoupled BL, where, apart from some subtle differences, the height-dependent organization of updrafts and downdrafts is the same.

Focusing first on thermodynamically coupled conditions, the percent of the strongest updrafts ( $>1 \text{ m s}^{-1}$ ) remained fairly constant from 200 to 900 m ( $\sim 5\%$ ), exhibited a rapid increase through the cloud layer to 1150 m ( $\sim 8\%$ ), and then decreased above that. The percentage of downdrafts stronger than  $-1 \text{ m s}^{-1}$  increased from the cloud top to its maximum of  $\sim 13\%$  at

900 m and decreased below it almost linearly during coupled conditions. During thermodynamically decoupled conditions, negligible amounts of updrafts stronger than  $1 \text{ m s}^{-1}$  ( $<1\%$ ) are observed and the percent of downdrafts stronger than  $-1 \text{ m s}^{-1}$  remained fairly constant from 200 to 1000 m ( $\sim 2\%$ ) and then peaked to a value of 5% at 1150 m with a decrease above that.

These data suggest the BL updrafts during decoupled conditions are organized in a manner that produce fewer updrafts that can transport water vapor from the surface to the cloud layer and that this reduction in the number of updrafts is increasingly extreme for the increasingly stronger updrafts, whereupon updrafts stronger than  $1 \text{ m s}^{-1}$  become nearly nonexistent. Consistent with the observation of negative skewness in these profiles (Fig. 11), there are a greater amount of updrafts than downdrafts because the downdrafts are narrow and intense and updrafts are broad and weak.

Averaged profiles of structurally coherent updrafts and downdrafts that span the depth of the BL (Fig. 13) show stark differentiation in which thermodynamically decoupled conditions possess notable symmetry between the updraft and downdraft profiles that are relatively devoid of accelerations, while coupled conditions exhibit large asymmetry and appreciable accelerations and decelerations. Constant vertical velocity profiles found in the decoupled condition probably reflect a

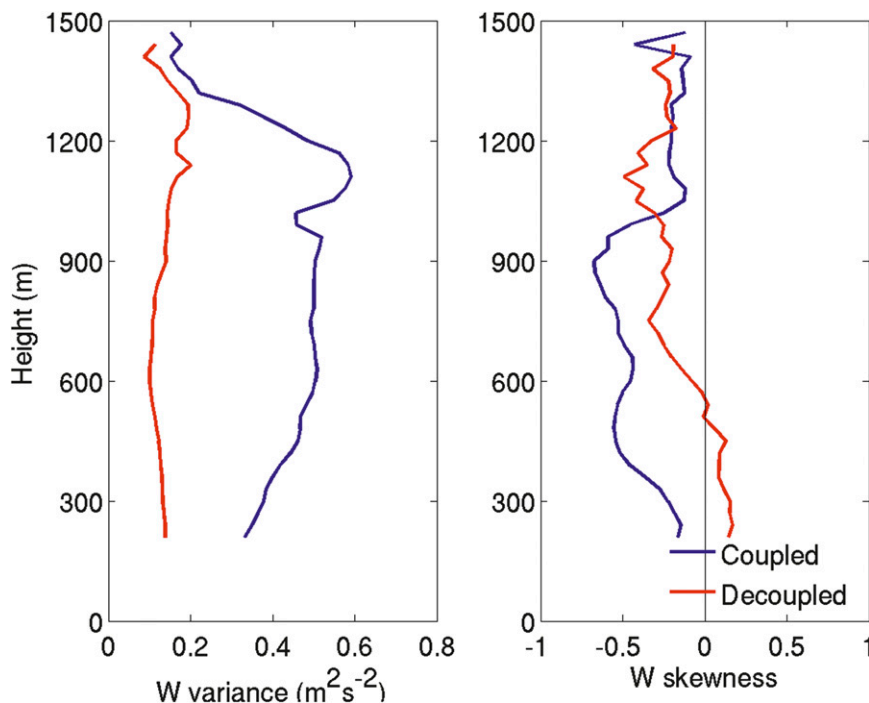


FIG. 11. Averaged profiles of (left) vertical velocity variance and (right) skewness during coupled and decoupled conditions.

small percentage of cases in which either 1) circulations in the subcloud layer and cloud layer are phase locked with the updrafts–downdrafts in the two layers occurring at the same time by chance or 2) the thermodynamic decoupling has been breached by a convective circulation fueled by the small amount of convective available potential energy (CAPE) that exists when the BL is decoupled. We would like to note that the existence of coherent updrafts and coherent downdrafts during decoupled conditions suggests some interaction between the two layers. A constant profile of the updraft vertical velocity during decoupled conditions suggests no acceleration due to CAPE.

During thermodynamically coupled conditions, the coherent downdrafts are accelerated as they move downward in the cloud layer and reach a maximum velocity in the vicinity of cloud base, and then they steadily decelerate as they sink toward the surface. Conversely, coherent updrafts during the coupled conditions move air steadily from the surface through the lower portion of the cloud, where it then experiences a rapid acceleration through a relatively shallow layer just above 1000 m before decelerating toward cloud top. The ratio of the coherent updrafts vertical velocity to the coherent downdrafts vertical velocity (not shown) in the middle of the BL was less than unity during coupled conditions, while it was closer to unity during decoupled conditions.

The updraft mass fluxes observed in thermodynamically coupled and decoupled conditions are vastly different, with the mass flux in coupled conditions being double of that in decoupled conditions in a majority of the BL. As in the case of the coherent drafts, the decoupled condition provides less structural variation in the mass flux as a function of height. Two distinct regions of relatively larger mass flux separated by a local minimum are noted in the coupled case: one maximum in the subcloud layer from 200 to 700 m at  $\sim 0.25 \text{ m s}^{-1}$  and another in the cloud layer peaking at around 1100 m. The position of the local minimum near the middle of the BL is probably due to its location relative to the energy sources that are driving the mass flux, which are located near cloud top and at the surface.

Mass fluxes binned by vertical velocity during coupled and decoupled conditions quantify the relative contributions of individual vertical velocity bins to the total mass flux (Fig. 14), which as previously noted was almost half of that during coupled conditions at all levels. Consistent with this reduced mass flux in decoupled conditions was a reduction in the vertical velocity of eddies responsible for the maximum transport compared to the coupled conditions in both updraft and downdraft regimes, yet there was little decrease in the actual mass transport caused by these eddies, especially in the downdraft regime. Updrafts stronger than  $1.5 \text{ m s}^{-1}$

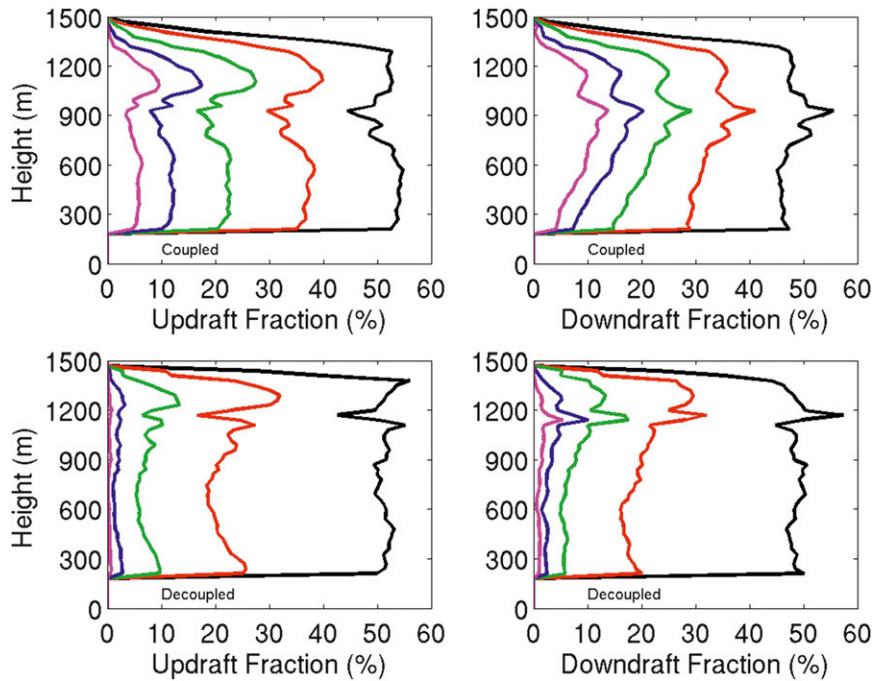


FIG. 12. (left) Updraft fraction and (right) downdraft fraction for (top) coupled and (bottom) decoupled conditions. The velocity thresholds are 0 (black), 0.25 (red), 0.50 (green), 0.75 (blue), and 1 (magenta)  $\text{m s}^{-1}$ .

are responsible for mass transports during the coupled conditions, while almost negligible transport is being done by updrafts stronger than  $1 \text{ m s}^{-1}$  during decoupled conditions. Significant mass transports are

done by eddies stronger than  $-1.5 \text{ m s}^{-1}$  in the downdraft regime during coupled conditions, while eddies stronger than  $-1.5 \text{ m s}^{-1}$  cause no transport during the decoupled conditions.

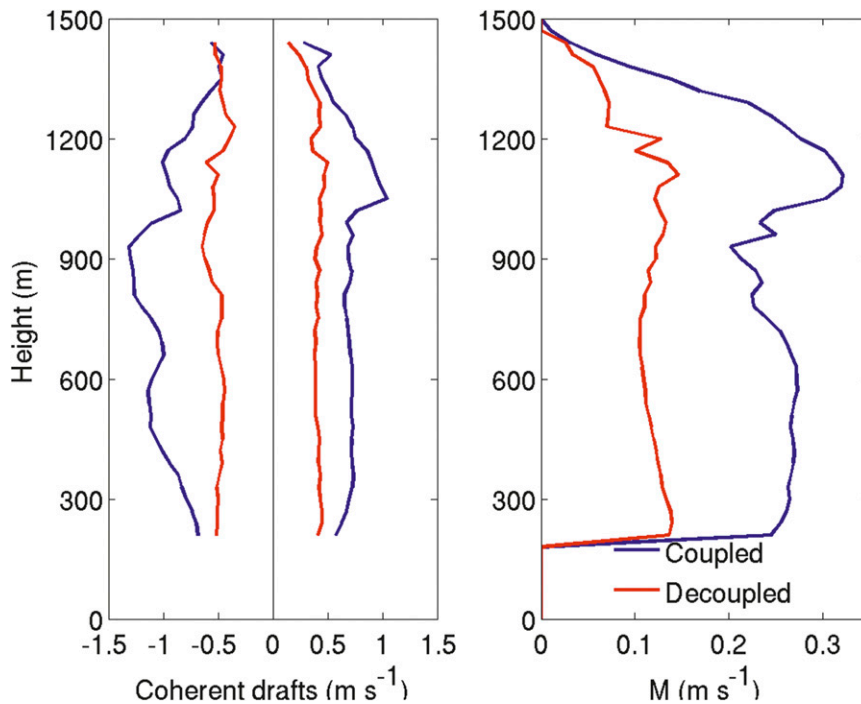


FIG. 13. Vertical profiles of (left) coherent updrafts and downdrafts, and (right) mass flux for coupled and decoupled conditions.

In past studies focusing on BL clouds, attempts have been made to use the convective velocity scale as a scaling parameter (e.g., Tjernström and Rogers 1996; Tjernström and Rune 2003; Neggers et al. 2007) so as to be ultimately used in prognostic parameterizations. The averaged profiles of vertical velocity variance, updraft mass flux, coherent updrafts, and coherent downdrafts scaled by the convective velocity scale  $w^*$ , discussed earlier, which takes into account the surface heating and radiative cooling of air parcels for the coupled and decoupled conditions, are shown in Fig. 15. The vertical velocity variance during coupled conditions was more than twice the vertical velocity variance during decoupled conditions at all levels (Fig. 11). When scaled by  $w^*$ , although the two variance profiles did not match with each other, the differences between them reduced at all levels. The averaged value of the ratio of vertical velocity variance to the square of velocity scale was 0.18 during coupled conditions and was 0.21 during decoupled conditions. The updraft mass flux did not scale well with  $w^*$ , with the ratio of updraft mass flux to the velocity scale being higher during decoupled conditions than during coupled conditions at all levels. The coherent updrafts spanning through the entire BL scaled well with the  $w^*$ , with the average value of the ratio of coherent updrafts to  $w^*$  of  $\sim 0.5$  during both coupled and decoupled conditions. The coherent downdrafts did not scale by  $w^*$  as remarkably as the coherent updrafts, but they exhibited some reduction in differences similar to the vertical velocity variance. The BL averaged value of the ratio of coherent downdrafts to  $w^*$  was 0.61 during coupled conditions and was 0.62 during decoupled conditions.

## 6. Summary and discussion

This study describes an analysis of data collected from multiple instruments as part of VOCALS-REx during a 24-h period on board the R/V *Ronald H. Brown*. This analysis is unique, to the best knowledge of the authors, for the first time coincident data from a vertically pointing Doppler cloud radar and Doppler lidar, both motion stabilized, that are combined to observe the turbulence structure of the entire stratocumulus-topped marine BL from cloud top to cloud base. These data are complemented by measurements of the LWP and IWV from a microwave radiometer and surface flux measurements.

The IWV, surface SHF, and surface LHF did not vary significantly during the 24-h study period, suggesting that changes in BL structure caused by advection of different air mass or changes in sea surface temperature were minimal. Radiative transfer model calculations

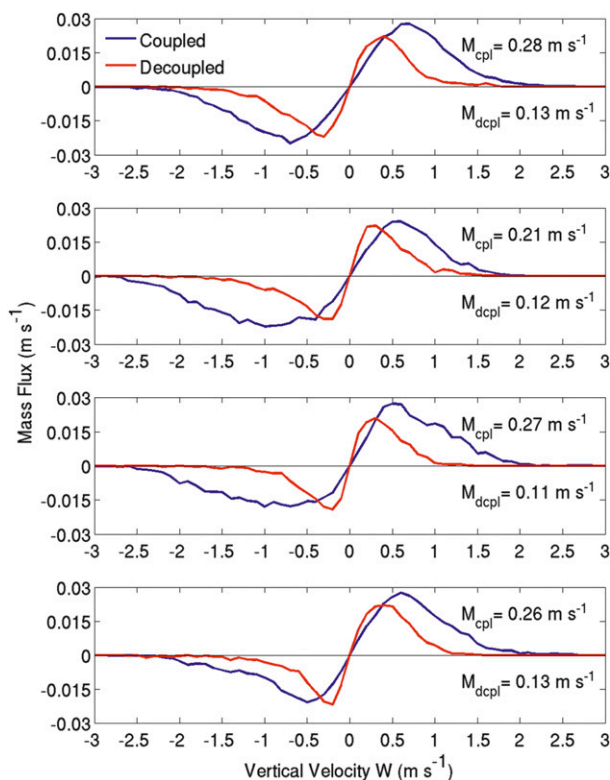


FIG. 14. Velocity binned mass flux (top to bottom) at 1200, 900, 600, and 300 m for coupled and decoupled conditions. The updraft mass flux for the distinction is also reported in each panel.

made at a high resolution showed an LW radiative cooling at the top of the BL during the entire period, which was more than entirely offset by the SW heating during the peak of the solar day. The surface buoyancy flux and the radiative flux divergence between the LCL and inversion base was also combined to formulate a convective velocity scale. Fourteen hours exhibited coupled BL conditions, with the LCL and cloud-base height differing by  $\sim 50$  m, while the remainder of the 24-h period exhibited decoupled BL with the LCL and cloud-base height differing by more than 200 m.

Mean values of all the variables along with the values averaged over the hours classified as coupled and decoupled are tabulated in Table 1. The surface air temperature, mixing ratio, wind speed, and wind direction did not change significantly during the study period, with small differences between them during the coupled and decoupled conditions. Cloud thickness was higher during the coupled BL conditions, and the average net radiative cooling near BL inversion base during decoupled conditions was  $\sim 42\%$  of that observed during coupled conditions. As hypothesized by previous studies, this net difference in radiative cooling is responsible (along with drizzle evaporative cooling) for decoupling of the

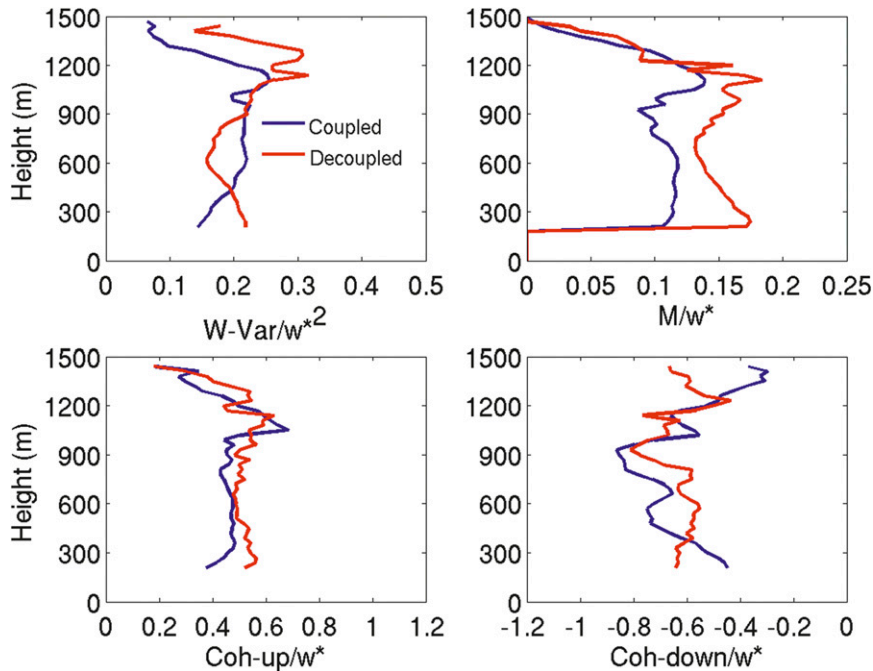


FIG. 15. Profiles of (top left) vertical velocity variance, (top right) updraft mass flux, (bottom left) coherent updrafts, and (bottom right) coherent downdrafts scaled by the convective velocity scale during coupled and decoupled conditions.

stratocumulus-topped BL. However, we have not made any attempts to evaluate the relative magnitude of reduction in cloud-top radiative cooling and drizzle-induced evaporative cooling in promoting decoupling of the BL. Our data demonstrate important structural differences in the turbulence profiles depending on thermodynamic structure: the average vertical velocity variance during decoupled conditions was only one-third of its value during coupled conditions.

Negative vertical velocity skewness was observed in both coupled and decoupled conditions in the cloud layer, but in the subcloud layer, smaller magnitudes of positive skewness were observed during decoupled conditions because of the decreased strength of downdrafts. Conditionally sampling the data to identify coherent vertical velocity structures that spanned the entire depth of the BL revealed the same relative relationship in negative skewness as present in the dataset as a whole. Philosophically, the notion of a “coherent” turbulence profile in decoupled conditions is rather counterintuitive since the basic definition of decoupling is based upon perceived incoherence in the turbulence profile. It is possible to reconcile this paradox if 1) circulations in the subcloud layer and cloud layer are phase locked or 2) the thermodynamic decoupling has been breached by a convective circulation fueled by the small amount of CAPE that exists when the BL is decoupled.

In either case, it is likely that the exchanges between the upper and lower portions of the BL when it is decoupled still occur during a small percentage of time (<5%).

Of paramount importance in this study is the characterization of the mass flux because its diagnosis is critical in the convective transports in models of all varieties, and it was determined that the updraft mass flux during coupled conditions was twice that during the decoupled conditions. Maximum transport of mass is accomplished in coupled conditions by eddies with vertical velocities between  $\pm 0.75$  and  $\pm 0.50 \text{ m s}^{-1}$  and in decoupled conditions by eddies with vertical velocities  $< 0.50 \text{ m s}^{-1}$ . Contemplating these results in the context of cloud formation suggests that these updraft velocities may limit the aerosol nucleation process in some circumstances, especially when the BL is decoupled. This latter possibility could potentially limit the magnitude of the Twomey effect during the daytime and, hence, mitigate or negate its impacts in this cloud system.

A proposed convective velocity scale, which takes into account the radiative cooling near BL top in addition to the surface buoyant production, was used as a scaling parameter for the dynamical properties. The vertical velocity variance and coherent downdrafts when scaled by the velocity scale had a similar value during the coupled and decoupled conditions. The coherent updrafts, which had a constant profile in the entire BL, also

scaled well with the velocity scale. This suggests that the proposed velocity scale could be used to calculate the strength of the coherent updrafts within the BL. Since the formulation of the velocity scale does not take into account the cooling induced by drizzle evaporation, consistent scaling of the coherent updrafts with  $w^*$  suggests that the coherent updrafts are little affected by drizzle evaporative cooling.

Our results highlight the differences in the turbulence structure of a stratocumulus-topped marine BL during coupled and decoupled conditions. While we have characterized the turbulence and radiation structure, we expect decoupling to be a result of the combination of reduction in the cloud-top radiative cooling and drizzle evaporative cooling, but the dominant process responsible for the decoupling and the cloud–radiation–turbulence coupling during this transition can only be further explored through an large-eddy-simulation-type model coupled to a bin microphysics scheme. Therein, we expect the results presented in this study to be helpful for future modeling and observational studies.

*Acknowledgments.* The authors thank the officers and crew of the NOAA ship *Ronald H. Brown* for great support during the cruise. Authors VG and MM were supported by the U.S. Department of Energy's Atmospheric System Research (ASR) program through Grants DE-SC0008584 and DE-FG02-08ER64531. This work was also supported by NOAA's Climate Project Office through the Earth System Science (ESS) program.

#### REFERENCES

- Ackerman, A. S., and Coauthors, 2009: Large-eddy simulations of a drizzling, stratocumulus-topped marine boundary layer. *Mon. Wea. Rev.*, **137**, 1083–1110.
- Arakawa, A., and W. H. Schubert, 1974: Interaction of a cumulus cloud ensemble with the large-scale environment, part I. *J. Atmos. Sci.*, **31**, 674–701.
- Bohnert, M., 1993: A numerical investigation of cloud-topped planetary boundary layers. Ph.D. thesis, Dept. of Mechanical Engineering, Stanford University, 338 pp.
- Bolton, D., 1980: The computation of equivalent potential temperature. *Mon. Wea. Rev.*, **108**, 1046–1053.
- Bony, S., and J.-L. Dufresne, 2005: Marine boundary layer clouds at the heart of tropical cloud feedback uncertainties in climate models. *Geophys. Res. Lett.*, **32**, L20806, doi:10.1029/2005GL023851.
- Bretherton, C. S., and M. C. Wyant, 1997: Moisture transport, lower-tropospheric stability, and decoupling of cloud-topped boundary layers. *J. Atmos. Sci.*, **54**, 148–167.
- , J. R. McCaa, and H. Grenier, 2004: A new parameterization for shallow cumulus convection and its application to marine subtropical cloud-topped boundary layers. Part I: Description and 1D results. *Mon. Wea. Rev.*, **132**, 864–882.
- , R. Wood, R. C. George, D. Leon, G. Allen, and X. Zheng, 2010: Southeast Pacific stratocumulus clouds, precipitation and boundary layer structure sampled along 20°S during VOCALS-REx. *Atmos. Chem. Phys.*, **10**, 10639–10654, doi:10.5194/acp-10-10639-2010.
- Caldwell, P., and C. S. Bretherton, 2009: Large eddy simulation of the diurnal cycle in southeast Pacific stratocumulus. *J. Atmos. Sci.*, **66**, 432–449.
- Comstock, K. K., R. Wood, S. Yuter, and C. S. Bretherton, 2004: Reflectivity and rain rate in and below drizzling stratocumulus. *Quart. J. Roy. Meteor. Soc.*, **130**, 2891–2918, doi:10.1256/qj.03.187.
- , C. S. Bretherton, and S. E. Yuter, 2005: Mesoscale variability and drizzle in southeast Pacific stratocumulus. *J. Atmos. Sci.*, **62**, 3792–3807.
- de Zoete, S. P., S. Yuter, D. Mechem, C. W. Fairall, C. D. Burleyson, and P. Zuidema, 2012: Observations of stratocumulus clouds and their effect on the eastern Pacific surface heat budget along 20°S. *J. Climate*, **25**, 8542–8567.
- Duda, D. P., G. L. Stephens, and S. K. Cox, 1991: Microphysical and radiative properties of marine stratocumulus from tethered balloon measurements. *J. Appl. Meteor.*, **30**, 170–186.
- Fairall, C. W., E. F. Bradley, J. E. Hare, A. A. Grachev, and J. B. Edson, 2003: Bulk parameterization of air–sea fluxes: Updates and verification for the COARE algorithm. *J. Climate*, **16**, 571–591.
- Feingold, G., A. Frisch, B. Stevens, and W. Cotton, 1999: On the relationship among cloud turbulence, droplet formation and drizzle as viewed by Doppler radar, microwave radiometer and lidar. *J. Geophys. Res.*, **104** (D18), 22 195–22 203.
- Frisch, A. S., D. H. Lenschow, C. W. Fairall, W. H. Schubert, and J. S. Gibson, 1995: Doppler radar measurements of turbulence in marine stratiform cloud during ASTEX. *J. Atmos. Sci.*, **52**, 2800–2808.
- Ghate, V. P., B. A. Albrecht, C. W. Fairall, and R. A. Weller, 2009: Climatology of surface meteorology, surface fluxes, cloud fraction, and radiative forcing over the southeast Pacific from buoy observations. *J. Climate*, **22**, 5527–5540.
- , —, and P. Kollias, 2010: Vertical velocity structure of non-precipitating continental boundary layer stratocumulus clouds. *J. Geophys. Res.*, **115**, D13204, doi:10.1029/2009JD013091.
- , M. A. Miller, and L. DiPreto, 2011: Vertical velocity structure of marine boundary layer trade wind cumulus clouds. *J. Geophys. Res.*, **116**, D16206, doi:10.1029/2010JD015344.
- Grund, C. J., and Coauthors, 2001: High-resolution Doppler lidar for boundary layer and cloud research. *J. Atmos. Oceanic Technol.*, **18**, 376–393.
- Hogan, R. J., A. L. M. Grant, A. J. Illingworth, G. N. Pearson, and E. J. O'Connor, 2009: Vertical velocity variance and skewness in clear and cloud-topped boundary layers as revealed by Doppler lidar. *Quart. J. Roy. Meteor. Soc.*, **135**, 635–643, doi:10.1002/qj.413.
- Jones, C. R., C. S. Bretherton, and D. Leon, 2011: Coupled vs. decoupled boundary layers in VOCALS-REx. *Atmos. Chem. Phys.*, **11**, 7143–7153, doi:10.5194/acp-11-7143-2011.
- Klein, S. A., and D. L. Hartmann, 1993: The seasonal cycle of low stratiform clouds. *J. Climate*, **6**, 1587–1606.
- Kollias, P., and B. A. Albrecht, 2000: The turbulence structure in a continental stratocumulus cloud from millimeter-wavelength radar observations. *J. Atmos. Sci.*, **57**, 2417–2434.
- , J. Rémillard, E. Luke, and W. Szyrmer, 2011: Cloud radar Doppler spectra in drizzling stratiform clouds: 1. Forward

- modeling and remote sensing applications. *J. Geophys. Res.*, **116**, D13201, doi:10.1029/2010JD015237.
- Liao, L., and K. Sassen, 1994: Investigation of relationships between Ka-band radar reflectivity and ice and liquid water contents. *Atmos. Res.*, **34**, 231–248.
- Lilly, D. K., 1968: Models of cloud topped mixed layers under a strong inversion. *Quart. J. Roy. Meteor. Soc.*, **94**, 292–309.
- Lock, A. P., and M. K. MacVean, 1999: A parameterization of entrainment driven by surface heating and cloud-top cooling. *Quart. J. Roy. Meteor. Soc.*, **125**, 271–300.
- Lothon, M., D. H. Lenschow, D. Leon, and G. Vali, 2005: Turbulence measurements in marine stratocumulus with airborne Doppler radar. *Quart. J. Roy. Meteor. Soc.*, **131**, 2063–2080, doi:10.1256/qj.04.131.
- Mather, J. H., S. A. McFarlane, M. A. Miller, and K. L. Johnson, 2007: Cloud properties and associated radiative heating rates in the tropical western Pacific. *J. Geophys. Res.*, **112**, D05201, doi:10.1029/2006JD007555.
- Mechem, D. B., S. E. Yuter, and S. P. de Szoeke, 2012: Thermodynamic and aerosol controls in southeast Pacific stratocumulus. *J. Atmos. Sci.*, **69**, 1250–1266.
- Medeiros, B., D. Williamson, C. Hannay, and J. Olson, 2012: Southeast Pacific stratocumulus in the Community Atmosphere Model. *J. Climate*, **25**, 6175–6192.
- Miles, N. L., J. Verlinde, and E. E. Clothiaux, 2000: Cloud droplet size distributions in low-level stratiform clouds. *J. Atmos. Sci.*, **57**, 295–311.
- Mlawer, E. J., and S. A. Clough, 1998: Shortwave and longwave enhancements in the rapid radiative transfer model. *Proc. Seventh Atmospheric Radiation Measurement (ARM) Science Team Meeting*, San Antonio, TX, U.S. Department of Energy, 409–413. [Available online at [http://www.arm.gov/publications/proceedings/conf07/extended\\_abs/mlawer\\_ej.pdf](http://www.arm.gov/publications/proceedings/conf07/extended_abs/mlawer_ej.pdf).]
- , S. J. Taubman, P. D. Brown, M. J. Iacono, and S. A. Clough, 1997: Radiative transfer for inhomogeneous atmospheres: RRTM, a validated correlated-*k* model for the longwave. *J. Geophys. Res.*, **102**, 16 663–16 682.
- Moeng, C.-H., and Coauthors, 1996: Simulation of a stratocumulus-topped planetary boundary layer: Intercomparison among different numerical codes. *Bull. Amer. Meteor. Soc.*, **77**, 261–278.
- Moran, K., S. Pezoa, C. W. Fairall, C. Williams, T. Ayers, A. Brewer, S. P. deSzoeke, and V. Ghate, 2012: A motion-stabilized W-band radar for shipboard observations of marine boundary-layer clouds. *Bound.-Layer Meteor.*, **143**, 3–24.
- Neggess, R. A. J., B. Stevens, and J. D. Neelin, 2007: Variance scaling in shallow-cumulus-topped mixed layer. *Quart. J. Roy. Meteor. Soc.*, **133**, 1629–1641.
- Stevens, B., C.-H. Moeng, and P. P. Sullivan, 1999: Large-eddy simulations of radiatively driven convection: Sensitivities to the representation of small scales. *J. Atmos. Sci.*, **56**, 3963–3984.
- Stull, R. B., 1988: *An Introduction to Boundary Layer Meteorology*. Kluwer Academic, 666 pp.
- Tjernström, M., and D. P. Rogers, 1996: Turbulence structure in decoupled marine stratocumulus: A case study from the ASTEX field experiment. *J. Atmos. Sci.*, **53**, 598–619.
- , and A. Rune, 2003: The structure of gradually transforming marine stratocumulus during the ASTEX first Lagrangian experiment. *Quart. J. Roy. Meteor. Soc.*, **129**, 1071–1100.
- Tomlinson, J. M., R. Li, and D. R. Collins, 2007: Physical and chemical properties of the aerosol within the southeastern Pacific marine boundary layer. *J. Geophys. Res.*, **112**, D12211, doi:10.1029/2006JD007771.
- Tucker, S. C., W. A. Brewer, R. M. Banta, C. J. Senff, and S. P. Sandberg, 2009: Doppler lidar estimation of mixing height using turbulence, shear, and aerosol profiles. *J. Atmos. Oceanic Technol.*, **26**, 673–688.
- Turton, J. D., and S. Nicholls, 1987: Diurnal variation of stratocumulus. *Quart. J. Roy. Meteor. Soc.*, **113**, 969–1009.
- Vali, G., R. D. Kelly, J. R. French, S. Haimov, D. Leon, R. E. McIntosh, and A. Pazmany, 1998: Finescale structure and microphysics of coastal stratus. *J. Atmos. Sci.*, **55**, 3540–3564.
- Wood, R., 2012: Stratocumulus clouds. *Mon. Wea. Rev.*, **140**, 2373–2423.
- , and Coauthors, 2011: The VAMOS Ocean-Cloud-Atmosphere-Land Study Regional Experiment (VOCALS-REx): Goals, platforms, and field operations. *Atmos. Chem. Phys.*, **11**, 627–654, doi:10.5194/acp-11-627-2011.
- Zhu, P., and Coauthors, 2005: Intercomparison and interpretation of single-column model simulations of a nocturnal stratocumulus-topped marine boundary layer. *Mon. Wea. Rev.*, **133**, 2741–2758.
- Zuidema, P., E. Westwater, C. Fairall, and D. Hazen, 2005: Ship-based liquid water path estimates in marine stratocumulus. *J. Geophys. Res.*, **110**, D20206, doi:10.1029/2005JD005833.